Bulletin of the Seismological Society of America, 90, 5, pp. 1143–1160, October 2000

The Athens Earthquake of 7 September 1999

by G-Akis Tselentis and Jiri Zahradnik

Abstract Based on detailed aftershock monitoring, the first model of the Athens earthquake is formulated, which is consistent with global, regional, and local strong-motion data of the mainshock, and fits with geological setting. The 30-station temporary network located 450 aftershocks. During the first 20 observation days the aftershocks identified the mainshock fault plane dipping 52° and striking 117°, consistently with the teleseismic fault-plane solution. A formal upward continuation of the fault plane intersects the surface close to the Fili fault. Numerical modeling of the broadband regional data at 10 stations (epicentral distances 140 to 370 km) estimates the centroidal source depth of 10 km and yields an average source duration of 5 to 6 sec. The interstation variability of the apparent duration indicates source directivity. The empirical Green's function modeling at the closest broadband station suggests a fault length of 20 or 10 km. Both the numerical and empirical modelings give a very short rise time of 0.1 to 0.3 sec. The short rise time seems to favor the nearly complete stress release of an asperity. A 10 km asperity (stress drop of 2.7 M Pa) is in agreement with a gap, identified during the first 12 observation days between two aftershock clusters. The strong-motion accelerograms in Athens also indicate a short apparent duration due to directivity (about 3 sec), and confirm an abrupt rupture beginning. There is no evidence for an abrupt stopping. The short rise time and short apparent source duration were two principal factors determining the damaging ground motions in Athens.

Introduction

On 7 September 1999, at 11:56:50 GMT an earthquake of $M_W = 5.9$ struck Athens, the capital of Greece. The intensity reached IX in the northwest outskirts of the city where 143 people were killed and more than 2000 were injured. Thirty-four people died in a four-story collapsed factory built on a slope of the Helidonou river valley. Many damaged houses were reinforced concrete structures constructed according the antiseismic code of 1978 (Fig. 1). For these and other engineering aspects, see web pages of EERI and ITSAK from where the strong-motion accelerograms can also be obtained (max 0.3 *g* at 20 km epicentral distance).

As a result of this disastrous event, more than 100,000 people remained homeless. There was neither major damage to lifelines nor secondary disaster caused by fires, chemical pollution, and so on. The earthquake was felt all over the city with intensities above VI. Historical monuments were nearly untouched except for small displacements at some columns.

Besides its societal importance, the earthquake also attracted attention because it occurred in one of the very few tectonically quiet parts of Greece. Indeed, neither historical records nor instrumental data show evidence of events *M* 5 or larger (Fig. 2) at distances smaller than 30 km from Athens (Papazachos and Papazachou 1997; Makropoulos *et al.,* 1989). There was no mapped fault marked as neotectonically active in the epicentral area.

The mainshock location parameters obtained from the Greek national network (National Observatory of Athens, NOA) and from global data (USGS) are summarized in Table 1. Both agencies located the event close to the damaged area. However, the differences between NOA and USGS epicenters and depths are 10 and 20 km, respectively. The three fault-plane solutions in Table 1 perfectly agree in showing normal faulting striking NWW–SEE. The USGS and Harvard complete moment tensor solutions suggest a nearly pure shear (double-couple) source mechanism. The trapezoidal source-time function derived from the Geophysical Laboratory of the University of Thessaloniki (GLUT) has a duration of 6 sec, with rise and fall times of about 1 sec (A. Kiratzi, personal comm., 1999).

A few days after the mainshock, the Seismological Laboratory of the Patras University deployed 30 temporary stations in Athens (Fig. 3). The aim of this article is to summarize the aftershock data obtained from 13 September to 28 October 1999, to supplement them by regional mainshock data, and to formulate a preliminary model of the Athens earthquake. The model will be discussed in relation with the

Figure 1. A typical example of structural damage (column failure followed by collapse) of a three-story residential reinforced-concrete building at about 8 km from the epicenter on soft soil.

known geological setting of the epicentral region and in connection to the major features of the strong-motion acceleration records.

Geology and Aftershocks

The epicentral region is located along the southeast-facing slopes of Mt Parnitha. The mountain block is made of Triassic–Cretaceous limestones that overlie Palaeozoic–Triassic shales and sandstones alternating with phyllites and quartz conglomerates. The prevailing tectonic structures within these rocks include EW- and NW-trending thrusts. Two SW-dipping normal faults dominate the neotectonic structure of this region: a N120°E striking fault referred to as Aspropyrgos fault and a N130°E fault referred to as Fili fault (Fig. 2). The Aspropyrgos fault is expressed as a prominent scarp that extends for 12 km and separates the limestone basement (to the north) and the plain deposits (to the south) where Athens is situated on. Parallel to this fault, and at 2 km and 4 km to the north, two other faults can be identified from the geological maps and satellite images (faults F2 and F3 in Fig. 2). Fault F3 is the most well known Fili fault that cut into the basement rock and forms a steep limestone escarpment reaching elevations of 100 m. No coseismic displacement due to the Athens earthquake was found on the listed faults. For more details, see the companion article (Tselentis and Zahradnik, 2000).

The local seismic network of the Seismological Laboratory of the Patras University, deployed a few days after the mainshock in and around Athens (Fig. 3), consisted of 30 stations. The distribution of the stations was designed with the following aims: (a) to locate aftershocks with enough precision allowing for correlation with existing faults (e.g., F1, F2, and F3 in Fig. 2) and to examine a possible migration of the aftershock activity to major nearby faults that have severely damaged Athens in the past (e.g., Atalanti and Thebes faults); and (b) to record aftershocks at various geological conditions within the epicentral region allowing for later investigations of site effects (not in this article).

Each station was equipped by a three-component 4 Hz SIG sensor, GPS receiver, and the 24-bit Earth data logger. The instruments have flat transfer function for velocity in the frequency range from 0.4 to 200 Hz. Most stations had sensors outside one- or two-story buildings, buried between 0.5 m and 1.0 m below the surface in specially constructed

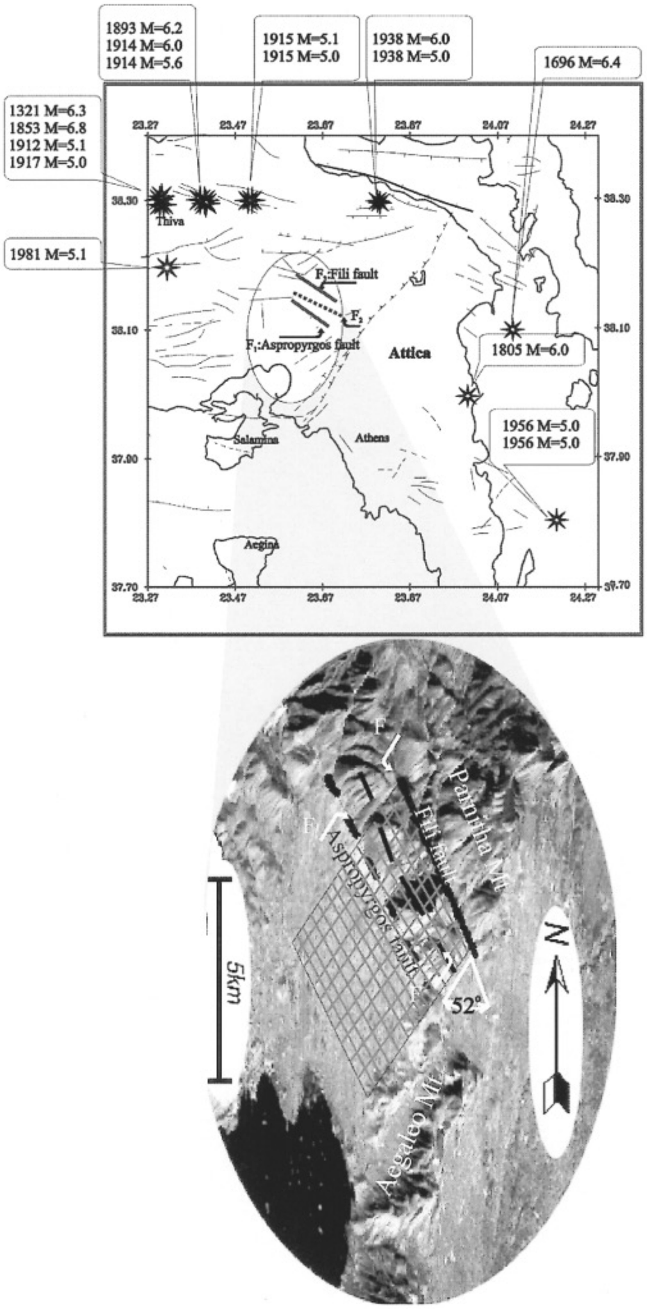

Figure 2. The seismicity around Athens ($M \geqq 5$), topography and tectonics. A schematic surface projection of the fault plane (discussed in this article) is included.

and cemented casings. The local geology is variable, and the underground structure is not well known. The instruments operated in a stand-alone regime with a continuous recording sampled at 200 Hz. The 2-GB disks were exchanged every five days. The processing comprised an automated event detection (Xanalatos and Tselentis, 1997), followed by manual picking of the *P*- and *S*-arrival times. Their estimated accuracy is 0.01 and 0.03 sec, respectively. The first-arrival polarity was also read. The coordinates of the stations and their altitudes were obtained from differential GPS measurements. All together, 450 events were processed, each one providing more than 40 *P* and *S* readings.

Table 1

Focal Parameters of the Mainshock by Various Agencies*

	Lat. (deg N)	Long. (deg E)	Depth (km)	Moment (Nm)	Strike (deg)	Dip (deg)	Rake (deg)
NOA	38.15	23.62	30	–	–	–	–
USGS	38.13	23.55	9	7.8e17	123	55	−84
Harvard	38.02	23.71	15	1.2e18	114	45	−73
GLUT	38.04	23.61	11–18	7.6e17	119	56	−82

*NOA, National Observatory of Athens; USGS, U.S. Geological Survey; Harvard, Harvard Centroid Moment Catalogue; GLUT, Geophysical Laboratory University of Thessaloniki.

A two-step method was used to locate the events: (a) the first approximation by HYPO71PC (Lee and Lahr, 1975) was followed by (b) a 3D grid search with structure optimization. An ad-hoc model used (Table 2) has a 900-m thick low-velocity layer of $V_P = 3$km/sec below the surface, reflecting the presence of Pleistocene sediments at most stations. The assumed velocity structure beneath the top layer is similar to the regional model M1 (Table 3), routinely used for many years by the Seismological Laboratory in Patras (Tselentis *et al.,* 1996a,b). The V_p/V_s ratio equals 1.78 everywhere. We considered location successful if the root mean squared (rms) residuals remained below 0.05.

Step (b), that is, the relocation by grid-search method (Jansky, 2000), begins with a definition of the target volume, comprising the hypocenters from step (a), with omission of outliers. The target volume is covered by a 3D grid of uniform 250 m increments in all three coordinates. For every event, the grid node is searched which minimizes the difference between the observed and calculated travel times. A homogeneous half-space was assumed, and the whole process was repeated with two free parameters: V_p (changing from 5.50 to 6.10), and V_p/V_s (from 1.750 to 1.875). The resulting misfit function calculated over all events and stations is depicted in Figure 4. The best solution was obtained for $V_p = 5.80$ km/s and $V_p/V_s = 1.800$. Compared to HYPO71, the rms travel-time residual averaged over all events decreased by a factor of 1.5.

We find a notable concentration of aftershock activity, mainly during the first 20 days of the recording period, when the epicenters tend to cluster in two groups. Later the two clusters approach each other and coincide (Fig. 5). Events near the eastern edge of the aftershock zone appear to have greater mean depth and to be more diffuse in space.

To study the depth distribution of the aftershocks and assess the geometry of the fault plane, the following method was employed: the hypocenters were projected into a vertical cross section perpendicular to the USGS mainshock strike (N 123°). Then the cross section was rotated to minimize the scatter of the foci. The best concentration of the hypocenters

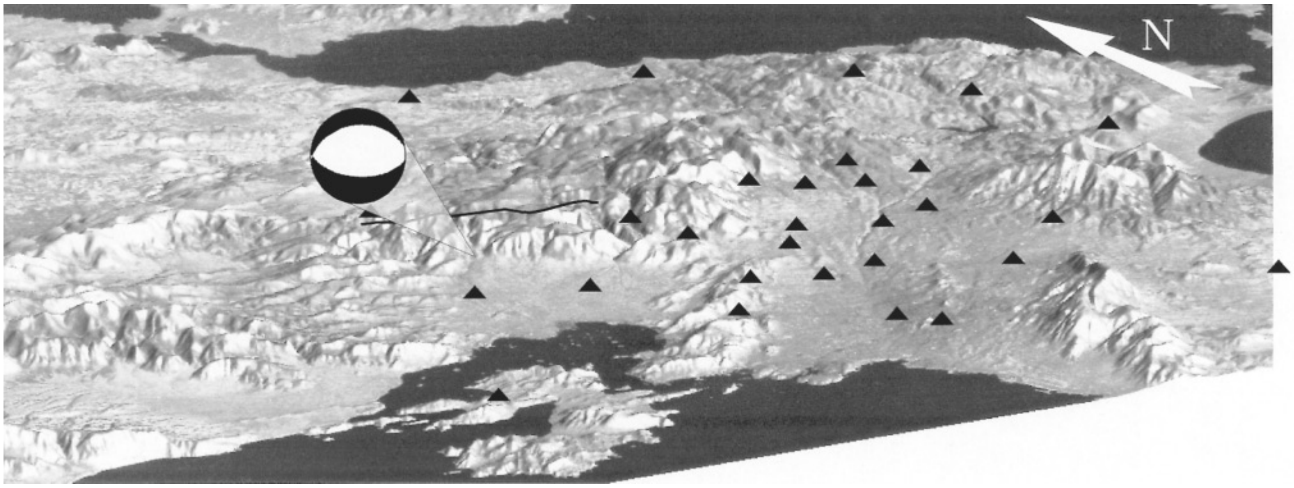

Figure 3. Temporary network (triangles) of the Patras University in and around Athens, superimposed on a topographic relief image. The seismogenic Fili fault (thick line) and the USGS focal mechanism are also depicted. The entire plot (including the 'beach ball') is rotated as shown by the North symbol.

Table 2
Crustal Model for the Aftershock Location by HYPO71*

Depth (km)	V_p (km/sec)
0.0	3.0
0.9	5.5
6.0	6.0
15.0	6.5
25.0	8.2

$V_p/V_s = 1.78$ everywhere.

Table 3
Regional crustal model M1*

Depth (km)	V_p (km/sec)
0.0	5.7
5.0	6.0
18.0	6.4
39.0	7.9

*$V_p/V_s = 1.78$ everywhere.

was obtained for the first 12 days of network operation, 14–25, September. Outliers were removed, and the data indicated grouping of the foci over two parallel planes. The main plane was fitted to the aftershock 3D distribution by the least-squares method. Figure 6 shows the resulting optimum cross section, perpendicular to the fault striking N 117°. The plane dips southward at 52°. Thus we conclude that the aftershocks agree well with the strike and dip of the USGS fault plane solution, and they clearly identify one of the two nodal planes as fault plane. The intersection of the fault plane with the Earth surface determines the so-called fault trace. Two arbitrary points on the surface defining the trace are: 38.159° N; 23.614° E, and 38.118° N; 23.716° E (Fig. 5). This direction coincides with the direction of the Fili fault (F3) mentioned previously (Fig. 2 and Fig. 5), suggesting that this was the main seismogenic fault. The other parallel fault indicated by the aftershock sequence when extrapolated toward the surface coincides with fault F2. On the other hand, no evidence of activation of the Aspropyrgos fault or migration towards the Atalanti and Thebes faults has been found.

Single-event fault plane solutions of 140 events have been determined following Reasenberg and Oppenheimer (1985). In most cases, the nodal planes are well constrained, and errors in strike, dip, and rake are usually less than 10°. A representative sample of the (lower-hemisphere) solutions in map view and cross-section is depicted in Figure 7. Most of the focal mechanisms show normal faulting on approximately east–southeast striking planes, in agreement with the focal mechanism of the main event. However, toward the east, the focal mechanisms tend to change to strike-slip faulting along northeast oriented planes, indicating activation of another series of faults following the direction of Aegaleo mountain. The root of this mountain might have acted as a boundary preventing further eastward activation of the Fili fault (B. Papazachos, personal comm., 1999).

Inferences about the Mainshock from SER Broadband Station (EGF Modeling)

Once we fix the strike and dip of the fault plane, the next issue is to resolve the size of the ruptured area and the position of the mainshock hypocenter. To this goal we search for such a rectangular fault zone (with the top and bottom edges presumably horizontal) whose projection onto the surface comprises the epicenters of the aftershocks. We concentrate again on the first 12 days only, because later the

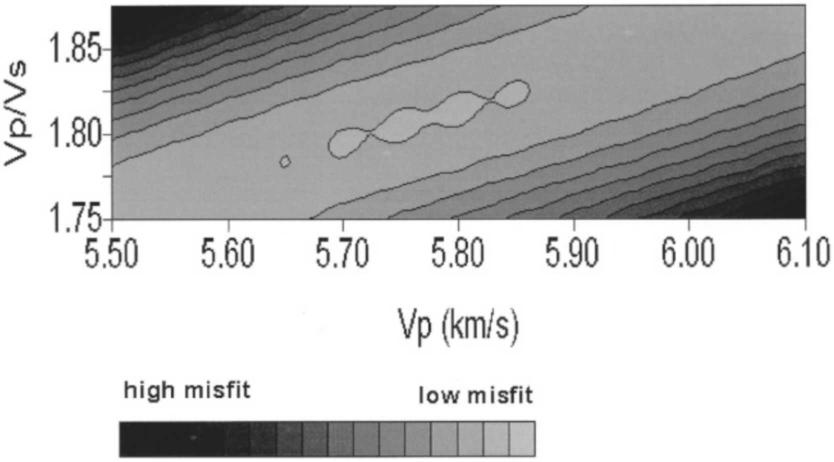

Figure 4. Minimization of the travel-time residuals by structure optimization. The misfit of the 3D grid-search location is shown as a function of V_p and V_p/V_s. The absolute minimum corresponds to $V_p = 5.80$ km/sec, and $V_p/V_s = 1.800$.

seismicity became more diffuse. This yields a rectangle whose length along the strike and width along the dip are $L = 20$ km and $W = 16$ km, respectively (Fig. 8). The NOA hypocenter does not fall into that zone because its depth is too large (30 km). The USGS hypocenter falls inside the inferred fault zone.

An interesting alternative is that the mainshock occurred just in a gap seen in the middle of the large rectangle of Figure 8, perhaps releasing all strain there, without aftershocks, or with some aftershocks before the installation of the network. This suggests another possible fault size, $L =$ 8 km and $W = 10$ km.

The closest three-component broadband station, Guralp CMG-3T, which recorded the Athens mainshock and the entire aftershock sequence, is the SER station at 38.413° N and 22.057° E; (Fig. 9). Station SER (whose former name was KALI) belongs to a small network that has been jointly operated by Charles University and Patras University in the western Corinth Gulf since 1997 (Zahradnik and Tselentis, 1999). The instrumental velocity response is flat from 0.01 to 50 Hz, sampled at 20 Hz continuously and at 100 Hz when triggered. The SER record of the Athens mainshock and an aftershock are shown in Figure 10. The mainshock peak velocity is just below the clipping level (2.3e–3 m/sec), thus the S/N ratio is excellent. The weaker event in Figure 10 is a magnitude 4 aftershock that occurred at 8 September 12:56, whose S/N ratio is good for frequencies greater than 0.1 Hz.

With the aim to study possible fault size and hypocenter position, ten different rupture scenarios were tested: The "small" fault, 8 × 10 km, with the hypocenter at its center, and nine "large" 20 × 16 km faults with variable position of the hypocenter (Fig. 11). These 10 scenarios were studied by the empirical Green's function method, EGF (Irikura and Kamae, 1994). Radial rupture propagation with constant velocity of 2 and 3 km/sec was tested, and (because of higher sensitivity with respect to hypocenter position) only the case of 3 km/sec is presented here.

Three parameters are needed for the EGF summation: the rise time (discussed subsequently); the ratio of the moments (mainshock versus aftershock), b; and the stress-drop ratio, c; The b and c parameters were obtained by fitting the low- and high-frequency flat parts of the Fourier amplitude spectral ratio of the two events by the omega-square model: $b = 150$, and $c = 1$ or 2, (Fig. 12). This method (Lindley, 1994), suggested to us by Ekstrom (personal comm., 1999), provides a significantly more reliable estimate of c than the separate stress-drop studies of the mainshock and aftershock from their corner frequencies. This is because the studied mainshock and aftershock spectra are strongly affected by structural path effects, thus peak frequencies of their velocity spectra have little or no relation to the source corner frequency. Having b and c, the assumed mainshock size tells us how many subevents must be summed up according to Equation (2.4) of Irikura and Kamae (1994), (Table 4).

Now we perform the EGF simulations for the scenarios described previously and compare them with the SER record. At this stage we also test the rise time (0.1 to 1.5 sec). First we consider the "small" fault (8 × 10 km), rupturing from its center (Fig. 13). The simulations well reproduce both long-period and short-period components of the observed signal for a rise time of 0.1 sec. For the two concurrent values of $c = 1$ and 2, a better fit was found for $c = 2$.

Next we study the "large" fault (20 × 16 km). The data again support a small rise time, with an optimum of 0.27 sec, but now with the stress-drop ratio $c = 1$. Among the nine models of Figure 14 the quantitative comparison of waveforms gives priority to scenario no. 2. Hypocenter no. 2 (Fig. 11) is in the middle of the top fault edge. Thus the optimum hypocenter of the "large" fault appears close to the hypocenter of the "small" fault.

We conclude that the EGF modeling with both "large" and "small" faults strongly suggests a small rise time (0.1–0.3 sec) as a prerequisite for simulating well the high-frequency content of the SER record. The size of the fault is not resolved well, that is, both the "large" and "small" faults are acceptable, mostly due to uncertain c. As a byproduct,

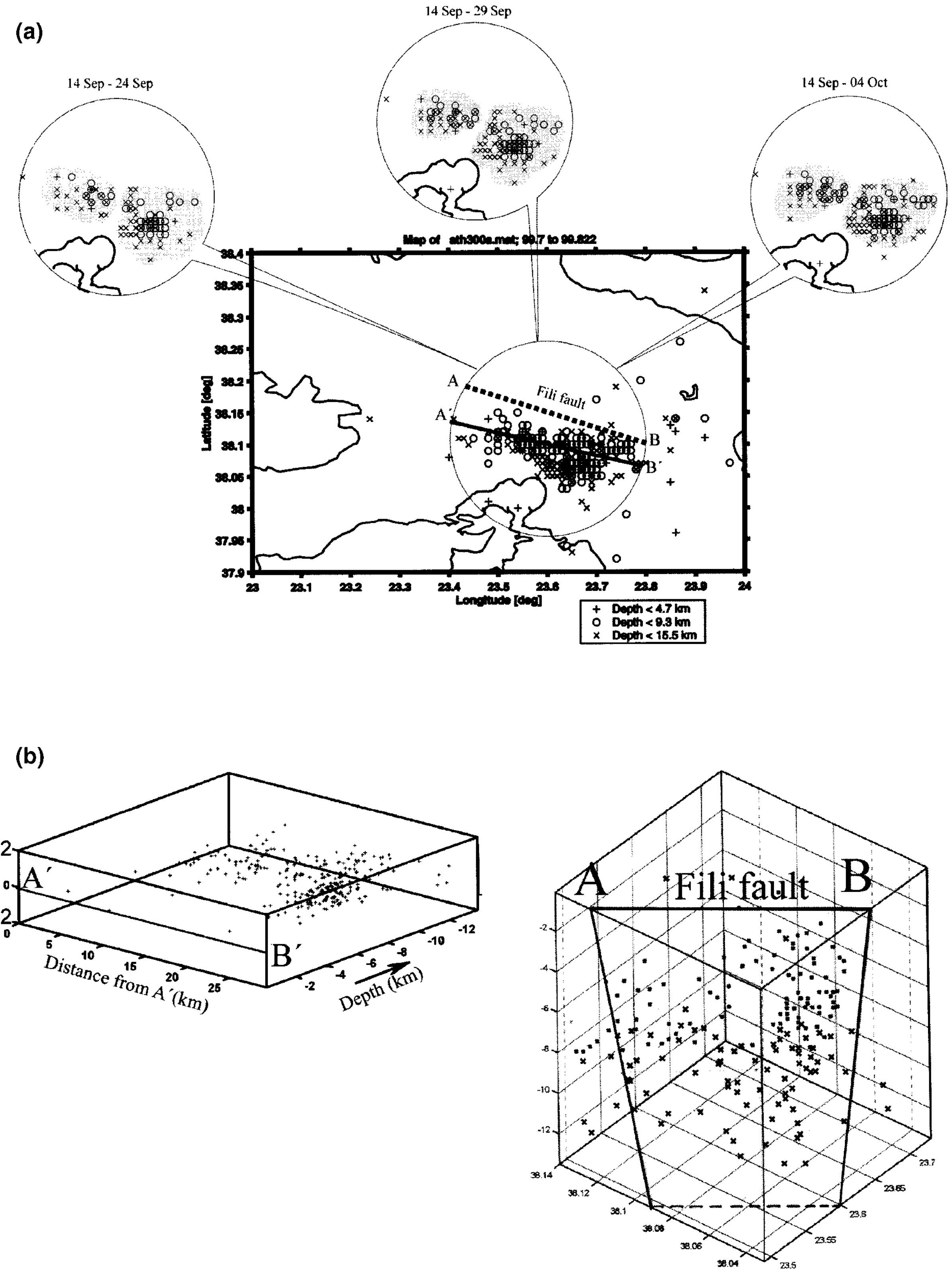

Figure 5. (a) Space and time evolution of the Athens earthquake aftershock sequence. The Fili fault is marked as AB. (b) Left: 3D vertical view along line A′B′ (the depth axis is horizontal, Right: 3D perspective view of the aftershock sequence and the Fili fault plane

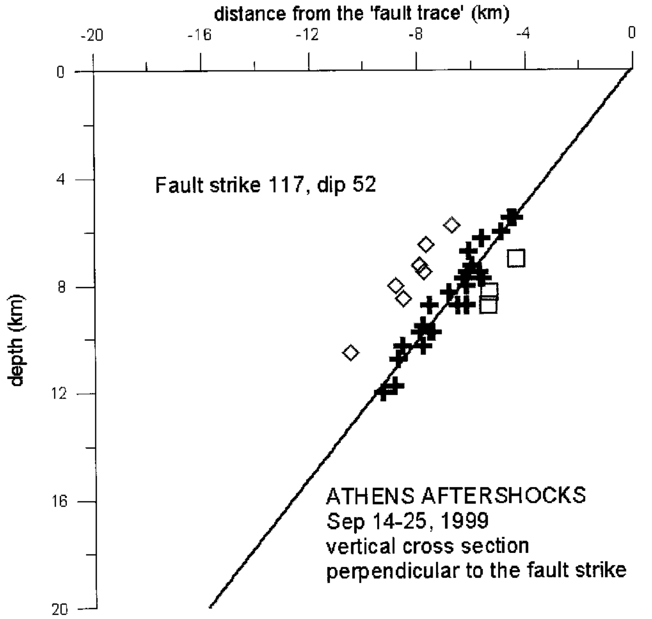

Figure 6. The aftershock distribution during the first 12 days in the cross section, which minimizes the scatter. The central cluster (crosses) identifies the fault plane striking at 117° and dipping at 52°. A formal extrapolation of the plane upward defines a theoretical surface "fault trace."

the mainshock stress drop of 0.34 and 2.7 M Pa is obtained for the "large" and "small" fault, respectively.

Inferences about the Mainshock from the Regional Broadband Network (DW Modeling)

Obviously, the source depth and size need verification from other stations. It is also needed to clarify if the high-frequency wave train superimposed on the low-frequency pulse is specific of the SER station, or is general, and from where it comes. This information can be obtained from the regional broadband (BB) data. To this goal, we process the mainshock records from nine stations of the Greek national network, operated by the National Observatory of Athens, NOA (Fig. 9). The stations are equipped with Lennartz LE-3D/20s sensors and Geotech DL-24 digitizers. Although the sensors are three-component, the multiplexed data available from NOA contain only horizontal BB components, while the vertical components come from a short-period Teledyne S-13 sensor (except station VAM, where the vertical component is also BB). In this study we employ only the BB velocity records of NOA, sampled at 50 Hz. These data are supplemented by the SER three-component BB record already discussed. Rotation into radial and transverse components according to the geometrical source-station azimuth is made.

We perform numerical modeling of the double-couple point source by the discrete wavenumber method, DW (Bouchon 1981; Kennett and Kerry, 1979; Coutant, 1989). Contrary to the EGF modeling, we need now a relatively good crustal model. Several models have been tested, and two typical ones are presented here: model M1 (Tselentis *et al.,* 1996a,b) and MA shown in Table 3 and 5, respectively. The topmost layer of model M1 is 5-km thick, with a relatively large value of $V_p = 5.7$ km/sec. Although successful for location purposes, this model fails in explaining prominent crustal surface waves in the regional BB stations.

Model MA is an ad-hoc model of this article developed by a trial-error modification from the previously published models featuring slow subsurface velocities. In particular, we began our search from models MN2 and MN3 (Tselentis *et al.,* 1986b; Plicka *et al.,* 1998), and removed their topmost layer ($V_p = 1.42$) which was needed for explaining local western Corinth Gulf events. Thus model MA ((Table 5) starts at the surface with $V_p = 2.67$ km/sec, continues with a velocity of 4.45 km/sec down to 5 km, and becomes identical to M1 below. A preliminary study of the Rayleigh and Love waves dispersion in Greece (Novotny, *et al.*, 2000). clearly prefers model MA compared to M1.

We work with the velocity time histories without any separation of phases. Robustness like that is typical of the DW method, where the complete seismic wave field is included automatically. The studied time window is 160 sec, time step is 0.02 sec, and the 8000 points are padded to 8192, resulting in a frequency step of 0.0061 Hz. We deal with the frequency range from 0.05 to 2 Hz. The Fourier amplitude spectra of the entire 160-sec window are compared with synthetic spectra for different models. The misfit is studied in the L2 norm: the squared amplitude residuals are summed up over all frequencies and averaged over all stations (except for the APE record excluded because of systematic anomalies, most likely caused by an overlapping nearby tremor). The radial and transverse components are processed separately. Modeling concentrates on the source depth and time function. The focal mechanism and the epicenter position have been fixed (the USGS solution, Table 1) because it has been validated by the aftershock distribution.

First we tested triangular time functions of different duration, but found little agreement between the observed and calculated spectra. Next trapezoidal time functions were used (with rise time and fall time equal to each other), and poor modeling results were still obtained,until choosing a rise time as small as 0.1–0.2 seconds. Finally we fix the rise time at 0.2 sec, and vary the length of the trapeziums from 4 to 8 sec (increment 1 sec), while simultaneously varying the source depth from 2.5 to 30 km (increment 2.5 km). The velocity inversion over the whole frequency range indicates a depth of 10 km. The most stable inversion results, mutually consistent for the radial and transverse components, were obtained when passing from the velocity spectra to the displacement spectra, and restricting the frequency range from 0.06 to 0.3 Hz (see the misfit functions in Figure 15).

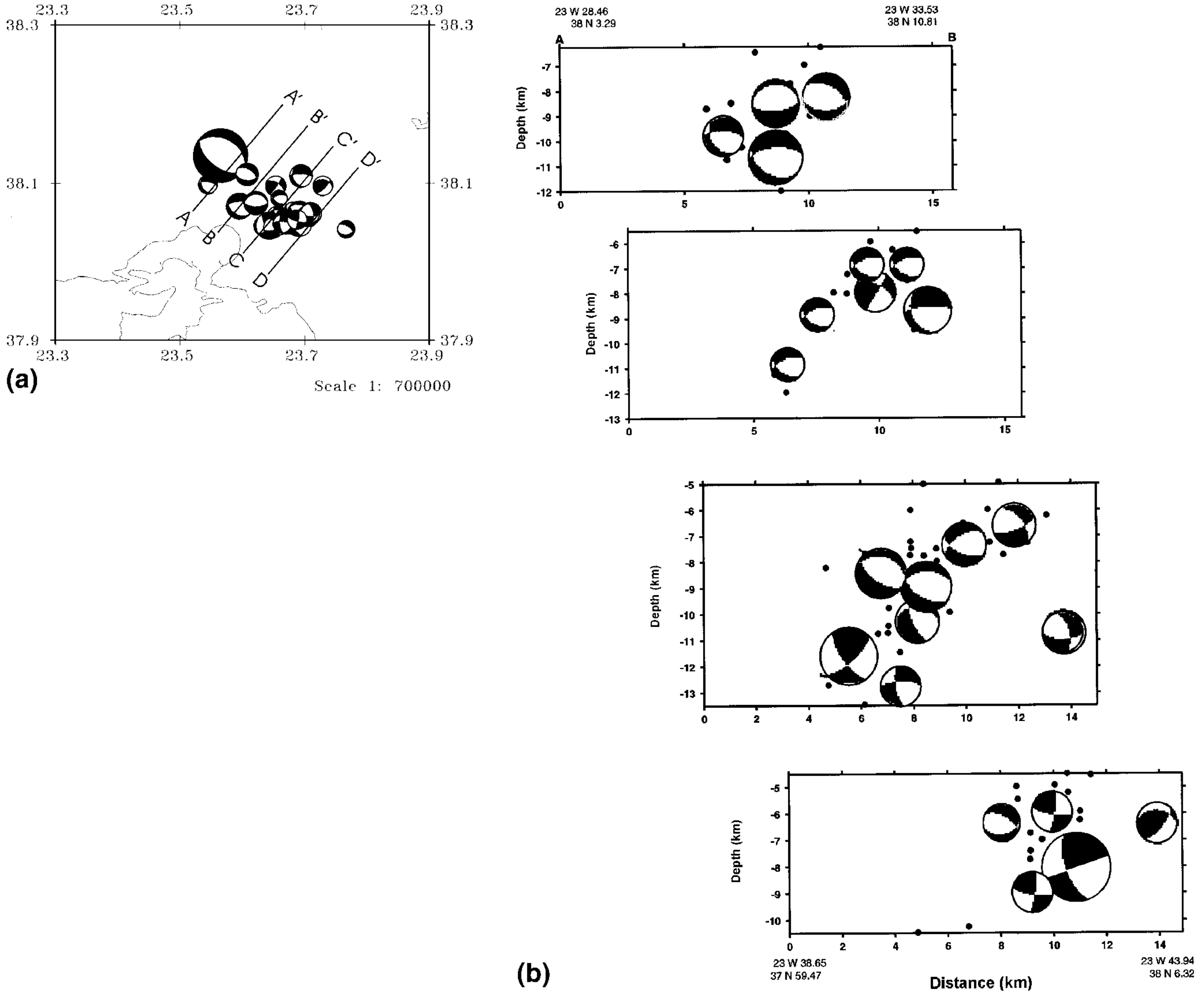

Figure 7. Single-event focal mechanisms. (a) Map view of the mechanisms and selected profiles A-A′, B-B′, C-C′ and D-D′ spaced every 5 km. (b) Depth cross sections along the profiles of panel a. The lower focal hemisphere is shown in both panels a and b.

The conclusion is that the regional data treated all together (on average) are best explained by a source depth of 10 km and a source duration of 5 to 6 sec. Using these parameters, the observed and calculated velocity spectra are compared up to 2 Hz in Figure 16. The overall agreement is reasonable, but its quality varies among the stations and components. That is why the stable inversion of the whole data set required the restriction to the low-frequency band.

The time-domain comparison displayed in Figure 17 shows that the best-fitting source parameters from the spectral inversion provide a fairly good explanation to such observed waveform features as peak velocities, duration, prominent long-period (10 sec) pulse-like crustal surface waves, and broadband body waves. The models reproduce the waveform complexity resulting from the strong interaction between the source and path effects. We can say that the structural and source effects ‘mask’ each other. That is why any attempt to interpret the regional broadband data in a more simplified manner, (e.g., using ‘corner frequencies’) would be dangerous, if not impossible. In contrast to the strong trade-off between the structure, depth, and duration, a single source feature has been clearly identified: the short rise time. A possible objection might be that the short rise time is an artifact of the employed absorption model (Q = 300 in the crust; Tselentis, 1993, 1997, 1998). However, an additional experiment in which we increased Q to 1000 everywhere below the depth of 2 km has confirmed that the data still require the small rise time.

Comparing the DW and EGF modelings we conclude that the DW point-source depth of 10 km, understood as an

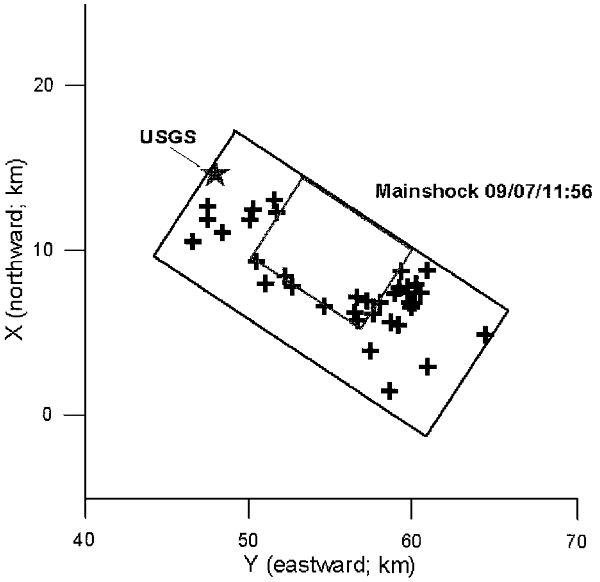

Figure 8. Epicenters of the aftershocks September 14–25, and the inferred fault contours projected onto the Earth surface. A large and small fault are considered. The USGS hypocenter is marked by the star.

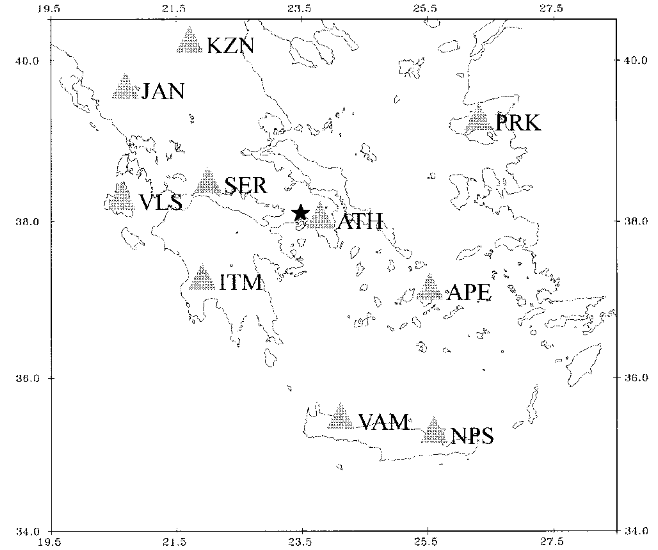

Figure 9. Broadband seismic stations used in this study (except RDO at 41.15° N and 25.54° E, which falls outside the digitized map). Star depicts epicenter of main event.

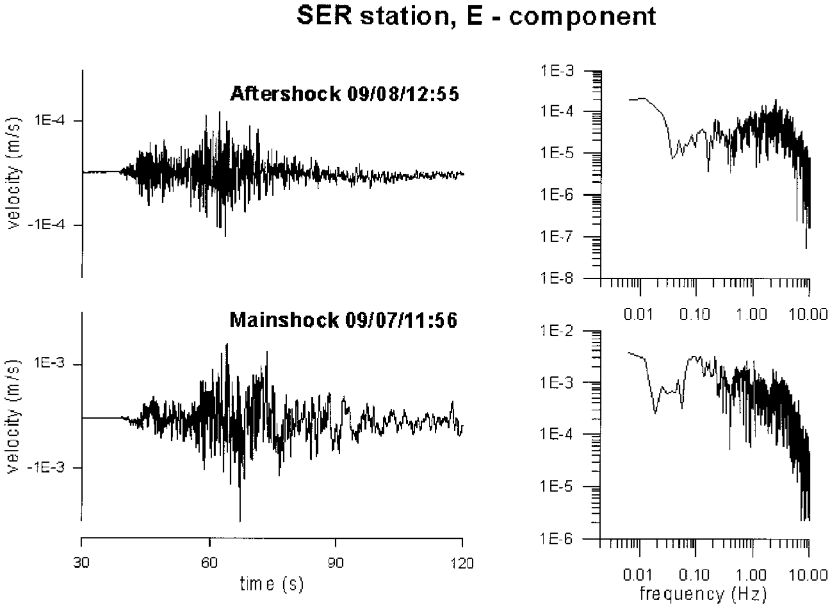

Figure 10. The Athens mainshock and a M 4 aftershock, recorded at SER broadband station (38.413°N and 22.057°E; epicentral distance 139 km, backazimuth 103 deg). Note different scales on the vertical axes of the mainshock and aftershock, respectively.

effective (centroidal) depth, is in agreement with the depth span of the EGF finite-extent fault models. The DW method seems to prefer an 'average' duration of 5 to 6 sec from all stations processed together. On the other hand, the large and small fault lengths resulting from the EGF simulations, 20 and 10 km, respectively, together with the successful rupture velocities 2 to 3 km/sec, yield a very uncertain duration estimate of 3 to 10 sec for the SER station. To clarify the latter, the empirical source-time function was deconvolved from the mainshock SER record (Mueller, 1985). The most stable result for the vertical component is consistent with the DW method estimate, 5 to 6 sec (Fig. 18). Fitting the amplitude spectral ratio between mainshock and aftershock suggests that the 6 sec symmetric trapezium of 0.2 sec rise- and fall-time provides a good fit good for the SER vertical component.

The aforementioned interstation variability of the fit between synthetic and observed data obviously stimulates an

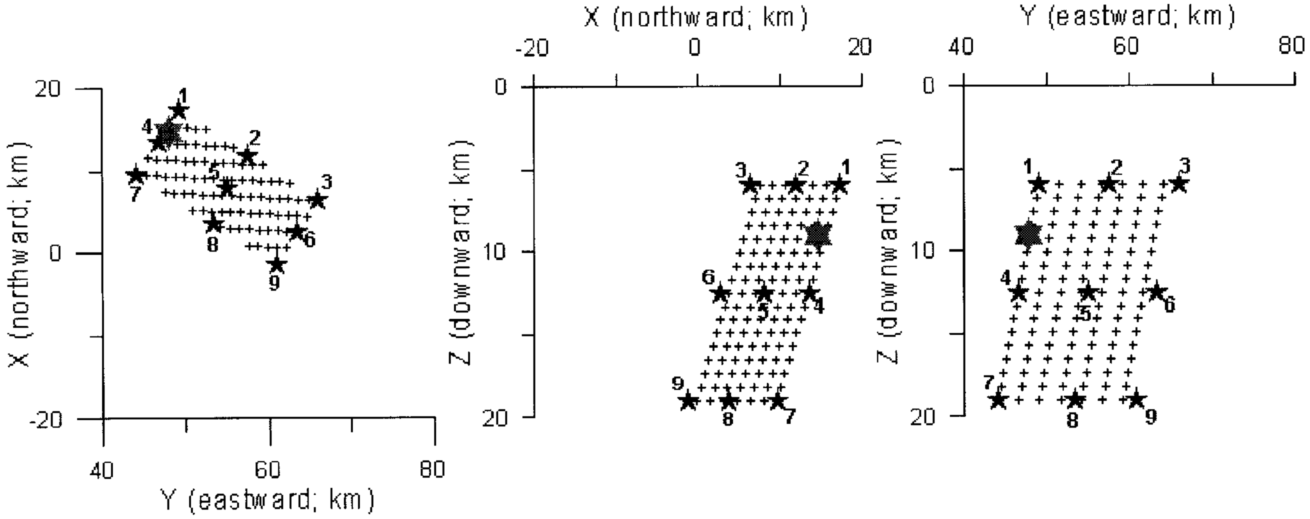

Figure 11. The fault plane and nine tested hypocenter positions marked by small stars. The big star is the USGS hypocenter.

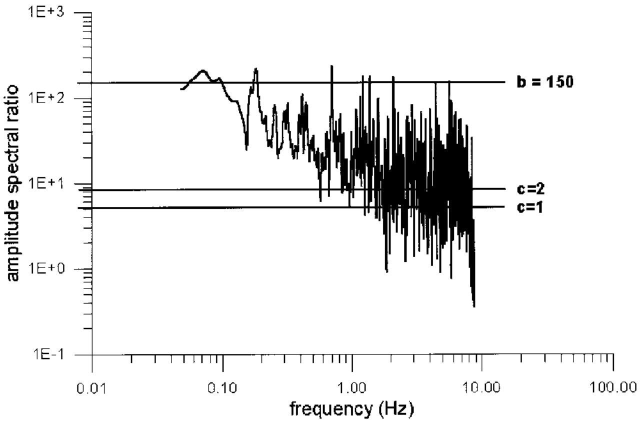

Figure 12. The amplitude spectral ratio (smoothed by a five-point running average) derived from the mainshock and aftershock records of Figure 10. Two constants needed in the EFG method, *b* and *c*, are fitted to the low- and high-frequency parts.

investigation of the apparent duration. To this goal we repeated the DW modeling (with fixed depth of 10 km), inverting the amplitude spectra for optimum duration at each BB station separately (Fig. 19). The radial component provides a more stable result than the transverse one, and indicates a directivity effect: shorter apparent duration (4–5 sec) toward NNE from the fault strike, and larger duration (7–8 sec) toward SSE. Thus the intermediate duration of 6 sec at SER, nearly on the fault strike, receives further support.

Table 4

Parameters of the EGF Simulation*

	L × W (km)	c	N × N	l × w (km)
"Large" fault	20 × 10	1	5 × 5	4 × 2
"Small" fault	8 × 10	2	4 × 4	2 × 2.5

**L*, *W*, fault length along strike and dip; *c*, stress-drop ratio mainshock versus aftershock; *N*, number of subfaults along strike and dip; *l* and w = subfault length along strike and dip.

Implications for Strong-Ground Motion in Athens

The question arises if a short rise time, strongly suggested by the regional BB records, and directivity (less strongly indicated) are in agreement with the observed strong-ground motions in Athens. To verify this, we have used the ITSAK SMA-1 accelerograms, whose peak accelerations at permanent stations ATH-2, 3, and 4 are 0.16, 0.30, and 0.12 *g*, respectively (Anastasiadis *et al.,* 1999). Lack of absolute time was compensated by the nearby NOA station ATH (Fig. 20), which recorded the mainshock on the short-period vertical component, and showed that the accelerographs were triggered by the *P* wave.

The epicentral distances of the strong-motion stations are about 20 km. With such a small distance, comparable to the fault size, the correct approach would be the finite-extent source modeling, considering different Green's functions for different parts of the fault. However, when trying to understand the features of the accelerograms by calculating the point-source impulse response of the medium (not shown here) we noticed that the observed accelerograms are short and simple enough, except at ATH-3, where most likely a significant site effect was present. This encouraged us to try

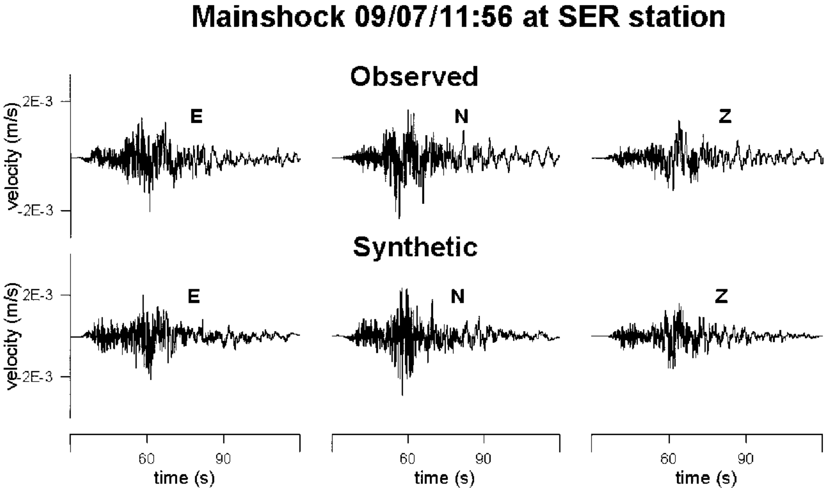

Figure 13. Comparison between the SER three-component record and the EGF synthetics for the best fitting small fault model (c = 2, rise time = 0.1).

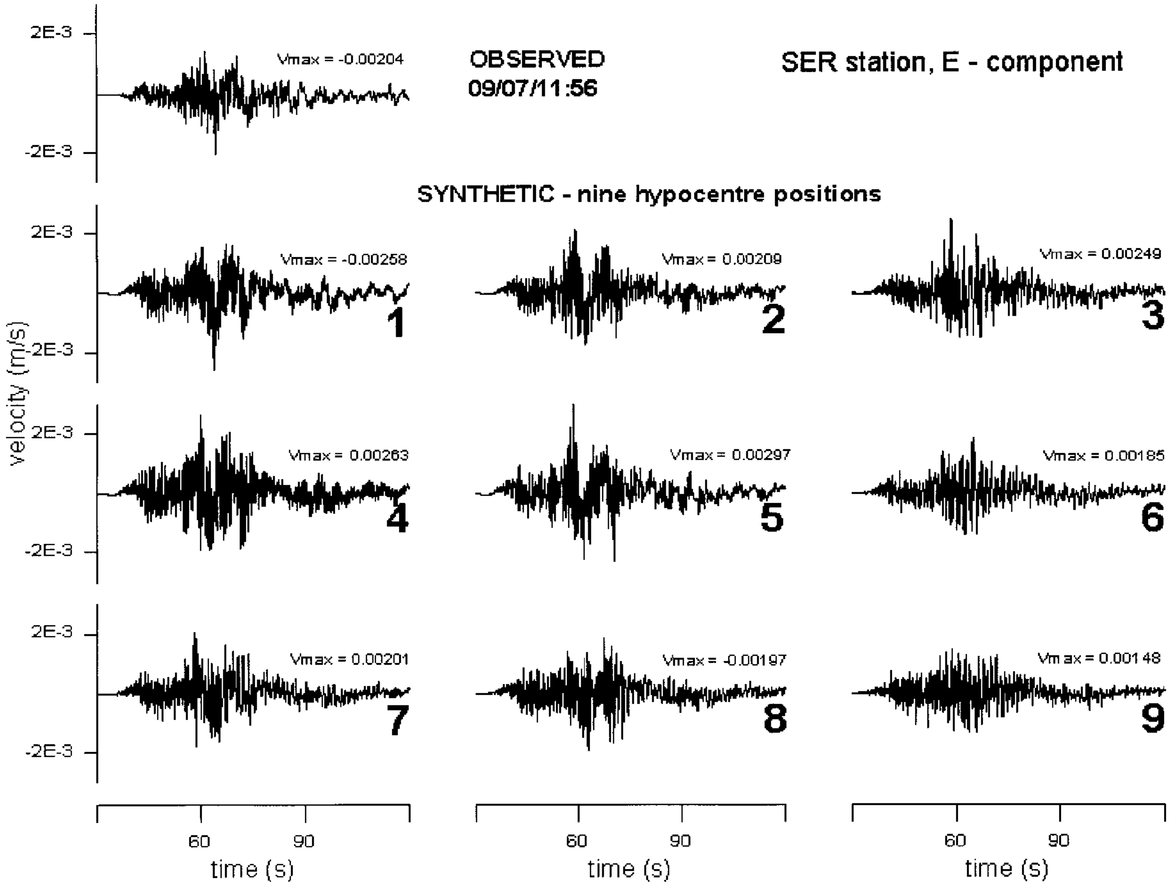

Figure 14. Comparison between the SER record (in the top left corner) and the EGF synthetics for nine tested hypocenter positions on the large fault (cf. Fig. 11).

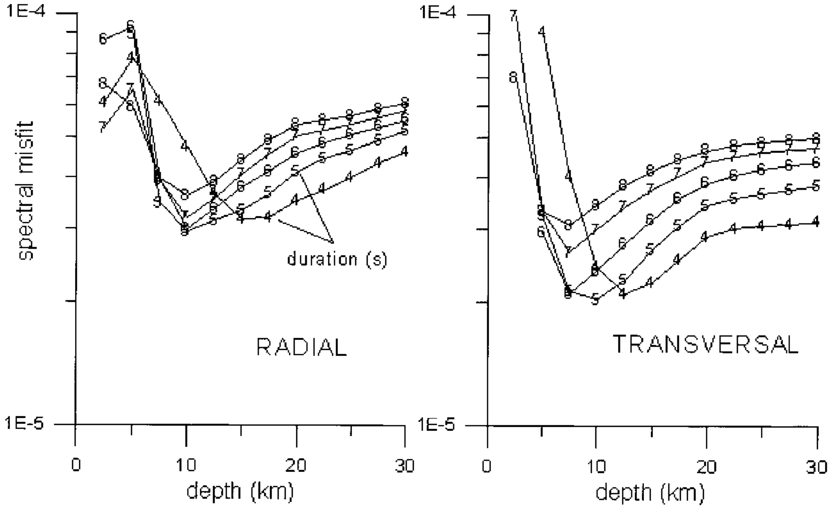

Figure 15. Misfit function of the DW modeling of the source depth and duration. The depth of 10 km and the duration of 5 to 6 sec has been preferred.

Table 5
Regional Crustal Model MA Preferred in the DW Modeling of This Article*

Depth (km)	V_p (km/sec)	Q
0.0	2.67	300
1.0	4.45	300
2.0	5.7	300
5.0	6.0	300
18.0	6.4	300
39.0	7.9	1000

*V_p/V_s = 1.78 everywhere.

the point-source DW modeling of ATH-2 and ATH-4 (similar to each other), employing various apparent source-time functions.

Using a rise time larger than 0.2 sec and/or a source duration longer than 4 sec resulted in the underestimation of the peak acceleration. Any attempt to use a symmetrical trapezoid with equally short risetime and falltime (0.1 or 0.2 sec) also failed, because the records do not exhibit two comparably strong starting and stopping phases, but the simulated peak acceleration values were reasonable. Finally, several models with asymmetrical trapezoid of 2.5 to 4 sec duration were quite successful, particularly those with risetime of 0.1 sec and falltime of 0.5 sec. Comparing the observed and synthetic accelerograms (Fig. 21), similarly low-pass filtered below 5.5 Hz, we obtain an excellent agreement for the radial component, that is, the same peak values, and a very similar waveform duration and envelope. Synthetics also well explain the single-pulse transversal component, but the peak value is (corresponding to the starting phase) is underestimated by the model.

The synthetic vertical component has stronger later arrivals than the observed one. Without modeling the site effects and the finite-extent source we can hardly provide any explanation for the fact that the radial component is modeled better than the other two. Anyway, most importantly, none of the observed components require larger rise time and/or stronger stopping phase as compared to those proposed by our model.

Our hypothesis is that the two most important factors resulting in large accelerations in Athens were: (a) the apparent source duration as short as 3 sec, caused by directivity, and (b) the prominent starting phase connected with the source rise time as short as about 0.1 sec. On the other hand, the data do not give any evidence for a strong stopping phase. The ongoing research should further clarify the finite-extent source effects and the local site effects and finally provide models explaining the damaging strong motions in the epicentral region not recorded by any instrument.

Conclusion

The 30-station temporary network, operated in Athens from 13 September until 28 October recorded 450 aftershocks, each one providing more than 40 *P* and *S* arrival-time readings. The two-step location method, based on HYPO and 3D grid search, has revealed that (a) during the first 20 days, the aftershocks concentrated between depths of 3.5 and 15.5 km along a fault plane dipping 52° and striking 117° (consistent with the mainshock fault-plane solutions inferred from teleseismic data). When formally extrapolated to the surface, the plane determines a "fault trace" that coincides with the Fili fault.

Numerical modeling of the regional broadband data at 10 stations (epicentral distances 140 to 370 km) provides an effective depth of 10 km, and a source duration of 5 to 6 sec if inverting stations together. Treating every station separately, shorter apparent source duration is found to the NNE of the fault (4 to 5 sec), and longer duration to the SSW (7 to 8 sec). At the closest broadband SER station, the empirical Green's function modeling suggested two possible fault lengths, 20 and 10 km. Both the numerical and empirical modeling indicate that the source process had a very short rise time, 0.1–0.2 sec.

The short rise time seems to prefer an asperity model with a nearly complete stress release. This idea is in agreement with a 10-km gap, identified during the first 12 observation days between two aftershock clusters. Therefore, from the two concurrent fault lengths discussed previously, 20 km and 10 km, we prefer the smaller one, which finally yields the mainshock stress drop of 2.7 MPa.

The strong-motion accelerograms in Athens indicate a very short apparent duration due to directivity (about 3 sec), and confirm an abrupt rupture beginning. On the other hand they do not provide any evidence for an abrupt stopping. Most likely, the short rise time and short apparent source duration were two principal factors determining the strong motions in Athens. More research is needed to clarify the interaction between the finite-extent source process and local site effects. It is believed that the continuing research will finally explain the seismic motions even in the most heavily damaged epicentral region, where no seismic stations operated during the mainshock.

Acknowledgments

The broadband records were kindly provided by the Geodynamic Institute of the National Observatory of Athens (NOA). The accelerograms were obtained from the Institute of Technical Seismology (ITSAK). G. Chouliaras (NOA) and N. Theodulidis (ITSAK) clarified technical details. GLUT data were kindly provided by S. Kiratzi and C. Papazachos. We thank T. Wright from Oxford University and I. Parharidis from Athens University for providing topographic relief data. Many colleagues and students collaborated during this study. Particular thanks go to T. Sokos, A. Sotiriou, G. Poulimenos, N. Martakis, O. Stavroulopoulou, S. Charalambopoulos, and A. Serpetsidaki (Patras Univ.) and J. Jansky, O. Novotny, V. Plicka, and O. Smrz (Charles Univ.). We also thank M. Bouchon, K. Kamae, and S. Gaffet for their thoughtful and constructive comments. The work was partly financed by: Meton Eter SA, The University of Patras Seismological Lab, The Earthquake Planning and Protection Organization of Greece, and the Charles University Grant 5/97/B.

References

Anastasiadis, An., M. Demosthenous, Ch. Karakostas, N. Klimis, B. Lekidis, B. Margaris, Ch. Papaioannou, C. Papazachos, and N. Theodulidis (1990). The Athens (Greece) Earthquake of September 7, 1999: Preliminary report on strong motion data and structural response, *http://www.itsak.gr/report.html*

Bouchon, M. (1981). A Simple Method to Calculate Green's Functions for Elastic Layered Media, *Bull. Seism. Soc. Am.* **71,** 959–971.

Coutant, O. (1989). Program of Numerical Simulation AXITRA. Res. Report LGIT, Grenoble (in French).

Earthquake Engineering Research Institute (EERI). *http://www.eeri.org/Reconn/Greece1099/Greece1099.html*

Harvard CMT catalog, *http://www.seismology.harvard.edu/*

Irikura, K., and K. Kamae (1994). Estimation of strong motion in broad-frequency band based on a seismic source scaling model and an empirical green's function technique, *Annali di Geofisica* **37,** 1721–1743.

Institute of Engineering Seismology and Earthquake Engineering (ITSAK). *http://www.itsak.gr*

Jansky, J. (1999). Grid Search Hypocentral Location Method in Simple I-D Media. *Acta Montana,* submitted.

Jansky, J., J. Horalek, J. Malek, and A. Bouskova (2000). Homogeneous velocity models of the West Bohemia swarm region obtained by grid search, *Studia geoph. et geod.* **44,** 158–174.

Kennett, B. L. N., and N. J. Kerry (1979). Seismic waves in a stratified half space, *Geophys. J. R. Astr. Soc.* **57,** 557–583.

Makropoulos, K. C., J. K. Drakopoulos, and J. B. Latousakis (1989). A revised and extended earthquake catalogue for Greece since 1900, *Geophys. J. Int.* **98,** 391–394.

Mueller, Ch. S. (1985). Source Pulse Enhancement by Deconvolution of an Empirical Green's Function, *Geophys. Res. Lett.* **12,** 33–36.

Lee, W. H. K., and J. C. Lahr (1975). HYPO71 (Revised): A Computer Program for Determining Hypocenter, Magnitude, and First Motion Pattern of Local Earthquakes, *U.S. Geol. Surv. Open-File Rep 85-749.*

Lindley, G. T. (1994). Source parameters of the 23 April 1992 Joshua Tree, California, Earthquake: its largest foreshock, and aftershocks, *Bull. Seism. Soc. Am.* **84,** 1051–1057.

National Observatory of Athens (NOA). *http://www.gein.noa.gr/services/*

Novotny, O., J. Zahradnik, and G-A. Tselentis (2000). Surface wave propagation from North-Western Turkey to the Corinth Gulf, Greece, European Seismological Conference 2000, Lisbon, 10–15 September.

Papazachos, B. C., and C. B. Papazachou (1997). *The Earthquakes of Greece,* Ziti Editions, Thessaloniki.

Plicka, V., E. Sokos, G-A. Tselentis, and J. Zahradnik (1998). The Patras earthquake (July 14, 1993): relative roles of source, path and site effects, *J. Seismology* **2,** 337–349.

Reasenberg, P., and D. Oppenheimer (1985). FPFIT, FPPLOT and FPPAGE: Fortran computer programs for calculating and displaying earthquake fault plane solutions, *U.S. Geol. Surv. Open-File Rep. 95-515,* 24 pp.

Tselentis, G-A. (1993). Depth dependent seismic attenuation in western Greece, *Tectonophysics* **225,** 523–528.

Tselentis, G-A. (1997). Evidence for stability in coda Q associated with the Eqion (Central Greece) Earthquake of 15 June 1995, *Bull. Seism. Sci. Am.* **87,** 1678–1684.

Tselentis, G-A. (1998). Intrinsic amd scattering attenuation in W. Greece.

Tselentis, G-A., N. Melis, E. Sokos, and K. Papatsimpa (1996a). The Egion June 15, 1995 (6.2 M_L) earthquake, western Greece, *Pure Appl. Geophys.* **147,** 83–98.

Tselentis, G-A., G. Koukis, E. Sokos, D. Rubas, J. Jansky, V. Plicka, M. Pakzad, and J. Zahradnik (1996b). Modelling the strong ground motions in the city of Patras, Greece, during July 1993 Earthquake, in *Proc. of the XI World Conference on Earthquake Engineering,* No. 127, 23–28 June 1996, Acapulco, Mexico.

Tselentis, G-A., and J. Zahradnik (2000). Aftershock monitoring of the Athens earthquake of 7 September 1999, *Seism. Res. Lett.,* **71,** 330–337.

U.S. Geol. Surv. (USGS) National Earthquake Information Center, World Data Center A for Seismology, *http://wwwneic.cr.usgs.gov/neis/FM/Q9909071156.html*

Xanalatos, N., and G-A. Tselentis (1997). SEISMWIN, an algorithm for processing seismological waveforms. *Proc. Geol. Soc. Athens* **22** 235–246.

Zahradnik, J., and G-A. Tselentis (1999). Broadband stations in western Corinth Gulf, ORFEUS Electronic Newsletter, *http://orfeus.knmi.nl/newsletter/vol1no3/index.html*

Seismological Laboratory
University of Patras
Rio 261 10 Greece
tselenti @upatras.gr
(G. A. T.)

Faculty of Mathematics & Physics
Charles University
Praha 121 16 Czech Republic
jz @karel.troja.mff.cuni.cz
(J. Z.)

Manuscript received 21 December 1999.

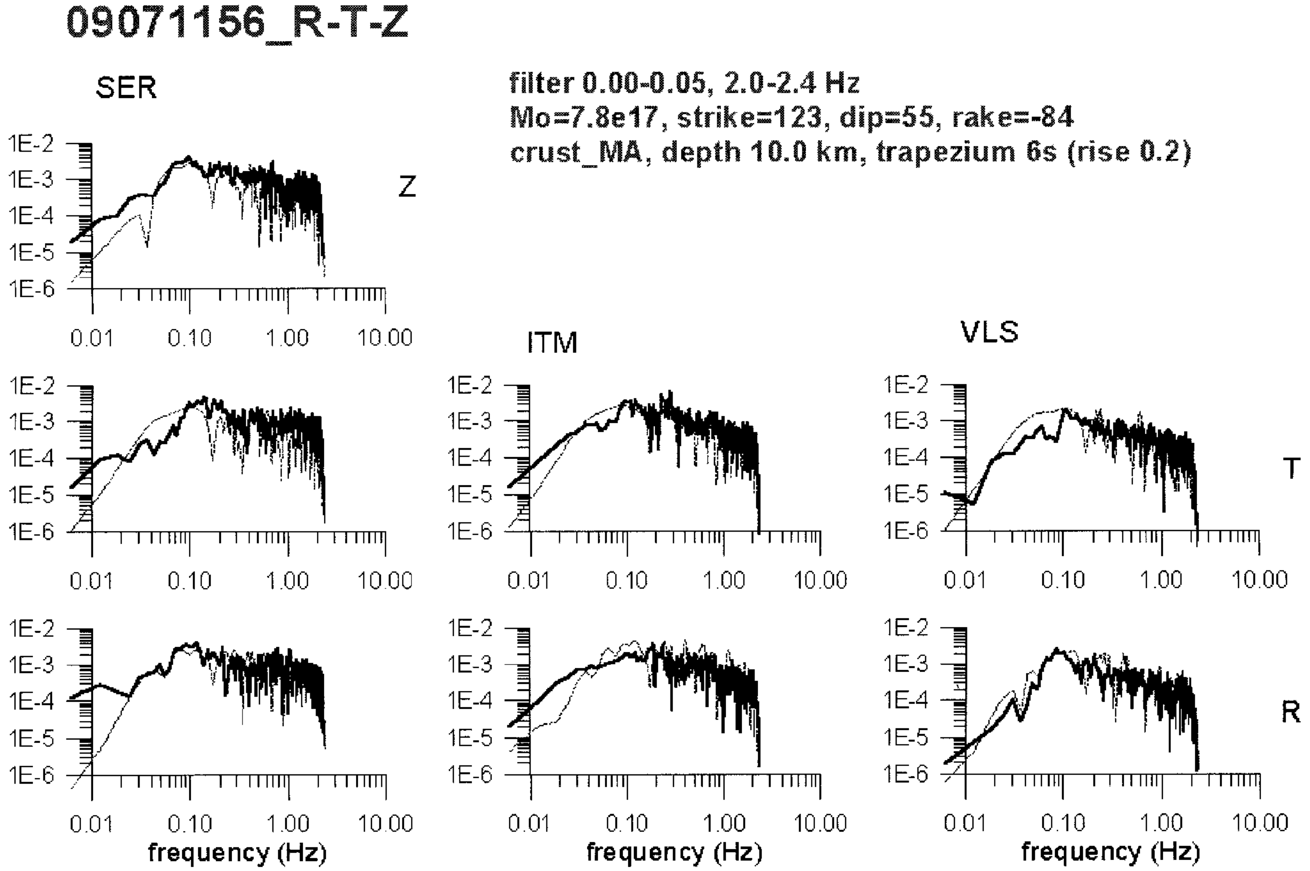
09071156_R-T-Z
filter 0.00-0.05, 2.0-2.4 Hz
Mo=7.8e17, strike=123, dip=55, rake=-84
crust_MA, depth 10.0 km, trapezium 6s (rise 0.2)
SER
ITM
VLS
Z
T
R
1E-2
1E-3
1E-4
1E-5
1E-6
0.01
0.10
1.00
10.00
frequency (Hz)

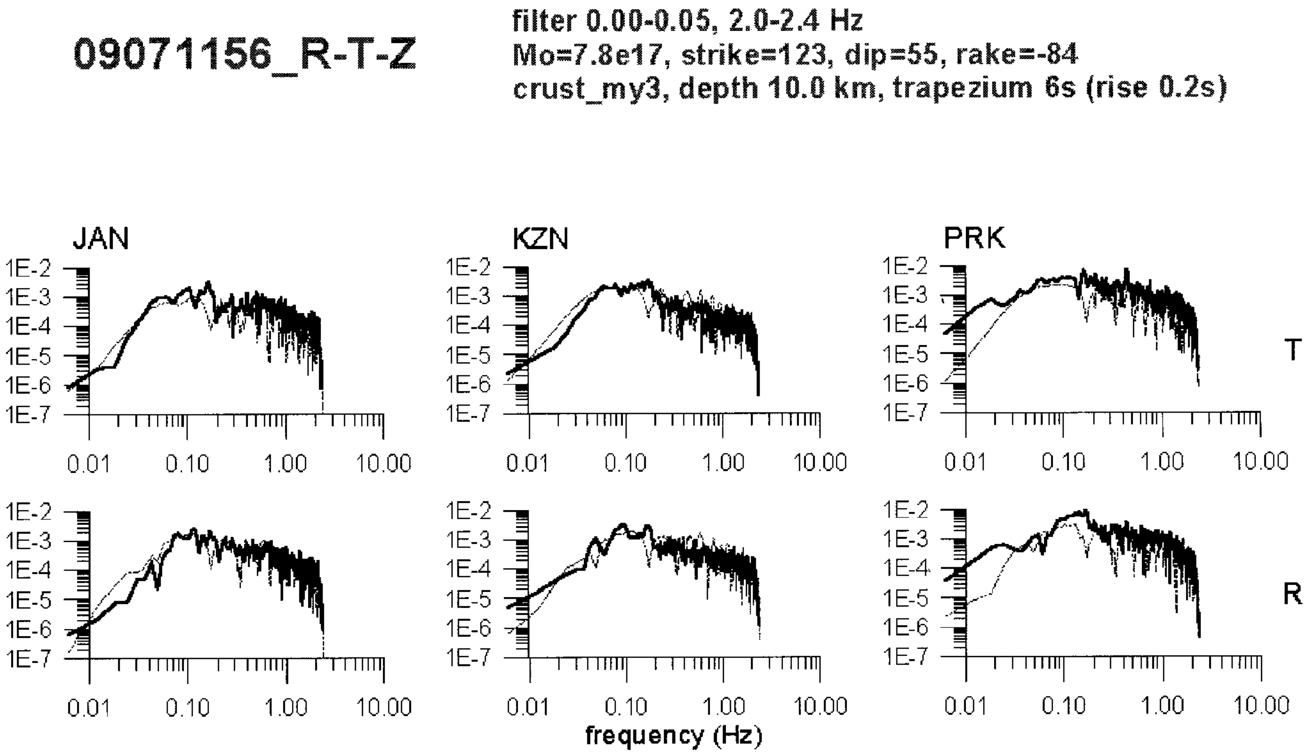
09071156_R-T-Z
filter 0.00-0.05, 2.0-2.4 Hz
Mo=7.8e17, strike=123, dip=55, rake=-84
crust_my3, depth 10.0 km, trapezium 6s (rise 0.2s)
JAN
KZN
PRK
T
R
1E-2
1E-3
1E-4
1E-5
1E-6
1E-7
0.01
0.10
1.00
10.00
frequency (Hz)

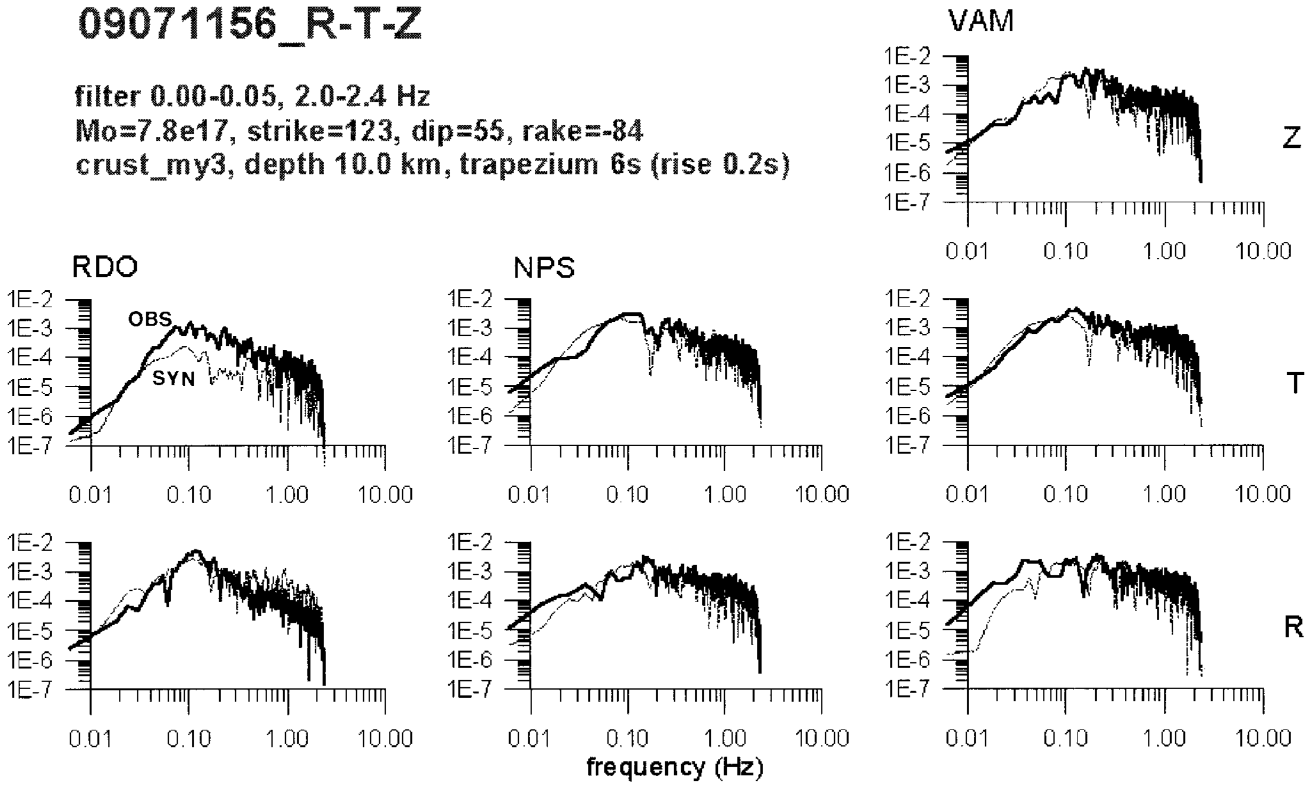

Figure 16. Comparison between the observed (thick) and calculated (thin) spectra for the source depth 10 km, duration 6 sec, and rise time 0.2 sec. The studied frequency range is 0.05–2.0 Hz.

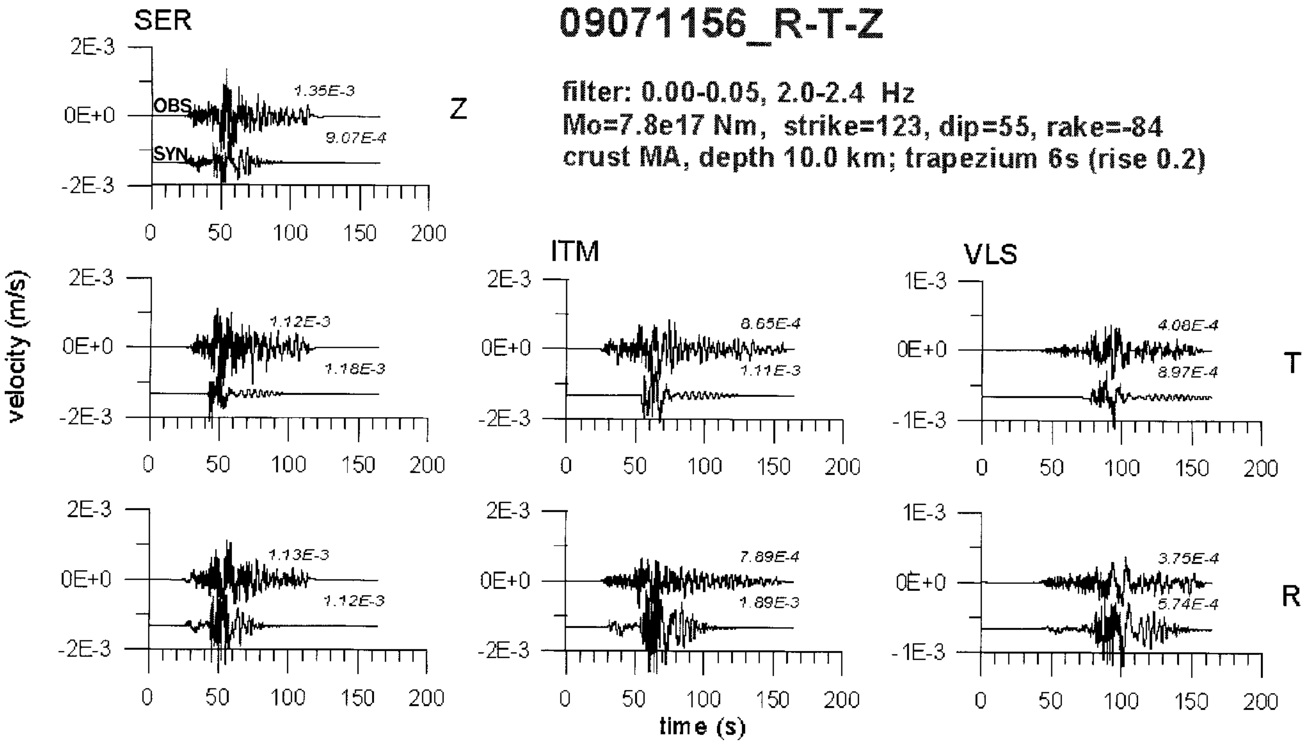
09071156_R-T-Z
filter: 0.00-0.05, 2.0-2.4 Hz
Mo=7.8e17 Nm, strike=123, dip=55, rake=-84
crust MA, depth 10.0 km; trapezium 6s (rise 0.2)
SER
OBS
SYN
1.35E-3
9.07E-4
Z
ITM
VLS
1.12E-3
1.18E-3
8.65E-4
1.11E-3
4.08E-4
8.97E-4
T
1.13E-3
1.12E-3
7.89E-4
1.89E-3
3.75E-4
5.74E-4
R
velocity (m/s)
time (s)
2E-3
0E+0
-2E-3
1E-3
-1E-3
0
50
100
150
200

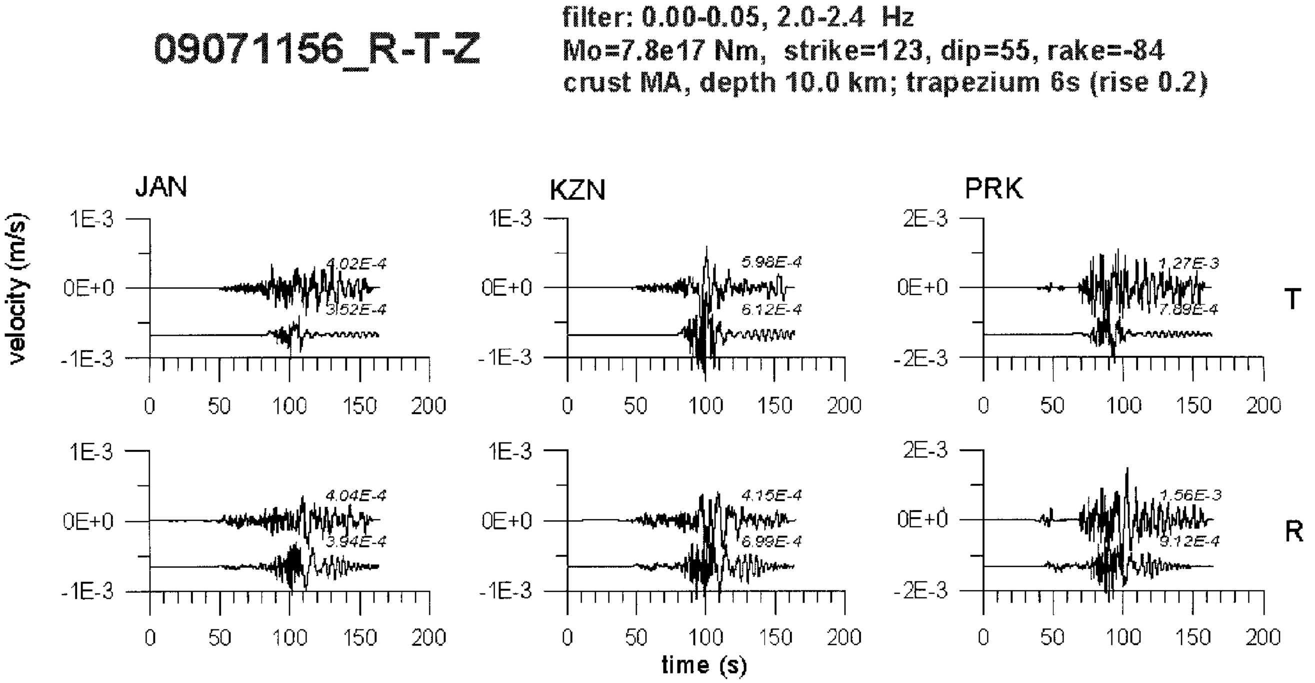
09071156_R-T-Z
filter: 0.00-0.05, 2.0-2.4 Hz
Mo=7.8e17 Nm, strike=123, dip=55, rake=-84
crust MA, depth 10.0 km; trapezium 6s (rise 0.2)
JAN
KZN
PRK
4.02E-4
3.52E-4
5.98E-4
6.12E-4
1.27E-3
7.89E-4
T
4.04E-4
3.94E-4
4.15E-4
6.99E-4
1.56E-3
9.12E-4
R
velocity (m/s)
time (s)
1E-3
0E+0
-1E-3
2E-3
-2E-3
0
50
100
150
200

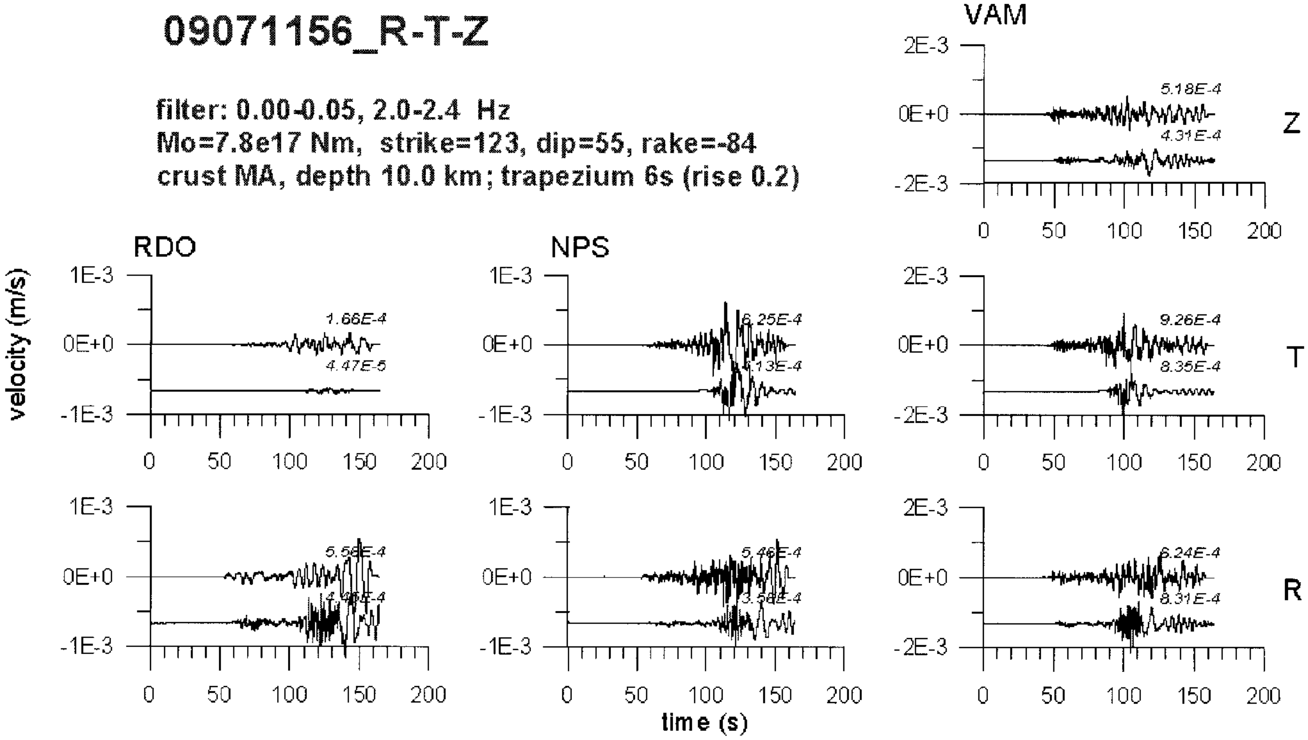

Figure 17. Comparison between the observed (thick) and calculated (thin) velocity time histories for the source depth 10 km, duration 6 sec, and rise time 0.2 sec.

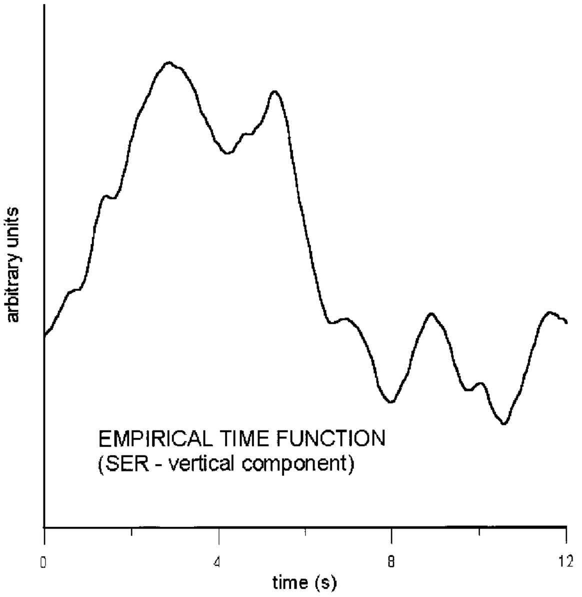

Figure 18. Empirical source-time function for SER station derived from the vertical components of the mainshock and aftershock of Fig. 10.

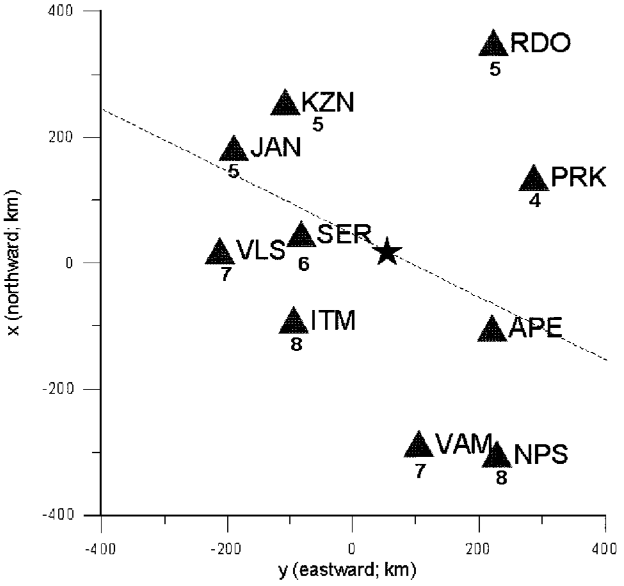

Figure 19. Apparent source-time function duration (numbers below triangles) for NOA stations and SER station. The fault strike is marked by dashed line.

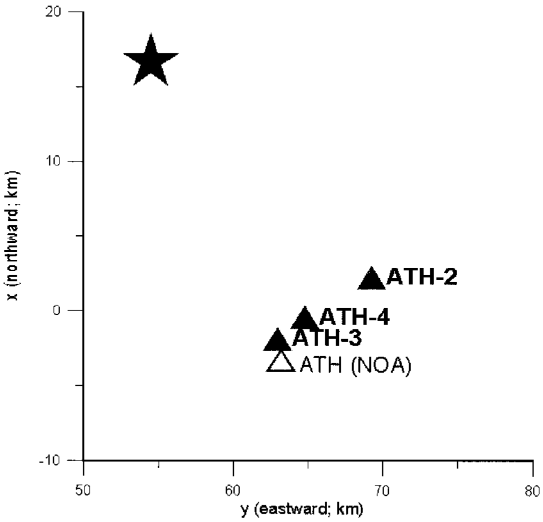

Figure 20. ITSAK permanent accelerograph stations (full triangles) that recorded the mainshock strong-ground motion in Athens. The epicenter is shown by star. The nearby NOA station ATH (open triangle) is also shown.

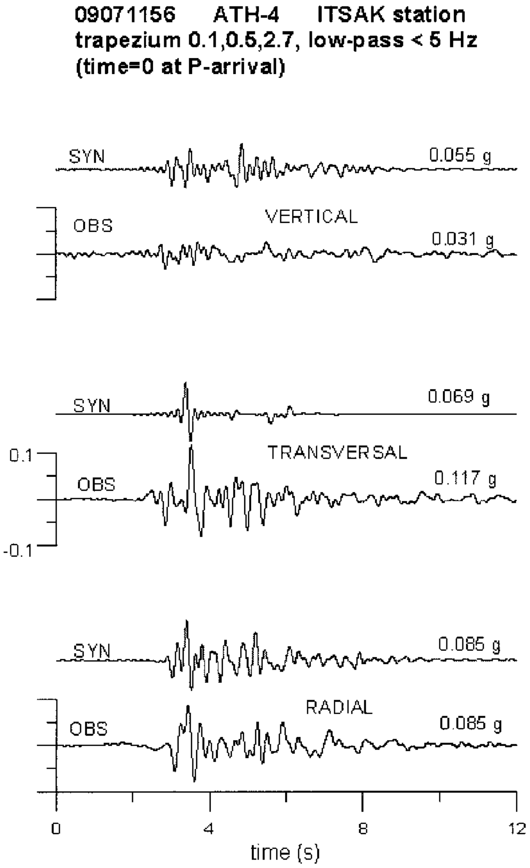

Figure 21. Comparison between the observed (thick) and synthetic (thin) strong-motion accelerograms at ITSAK station ATH-4. The best fitting apparent source time function is an asymmetrical trapezium of the whole duration 2.7 sec, short rise time (0.1 sec), and long fall time (0.5 sec).